Supporting Information

Large-scale Production of Graphene Nanoribbons from Electrospun Polymers

Nan Liu,[†] Kwanpyo Kim,[†,⊥] Po-Chun Hsu,[‡] Anatoliy N. Sokolov ,[†,Δ] Fung Ling Yap,[†,#] Hongtao Yuan,[§,∥] Yanwu Xie,[§,∥] Hao Yan,[‡,∥] Yi Cui,[‡,∥] Harold Y. Hwang,[§,∥] and Zhenan Bao[,†]*

[†]*Department of Chemical Engineering,* [‡]*Department of Materials Science and Engineering, and* [§] *Geballe Laboratory for Advanced Materials, Department of Applied Physics, Stanford University, Stanford, California 94305, United States*

[∥]*Stanford Institute for Materials and Energy Sciences, SLAC National Accelerator Laboratory, Menlo Park, California 94025, United States*

[⊥]*Department of Physics, Ulsan National Institute of Science and Technology (UNIST), Ulsan 689-798, Korea*

[#]*Institute of Materials Research and Engineering (IMRE), Agency for Science, Technology and Research (A * STAR), Research Link, 117602 Singapore*

[Δ]Current address: The Dow Chemical Company, Midland, MI 48674, United States

This file contains:

- Experimental section
- Additional supporting information

1. Optimization of the synthetic conditions for polymer-templated GNRs
2. CVD growth on Pd@PS nanofibers
3. The role of PVP
4. Width comparison of electrospun polymer and GNRs at different concentrations of Pd catalysts
5. Elemental analysis
6. Comparison of graphitization degree at different Pd^{2+} concentrations
7. Removal of Pd nanoparticles
8. Analysis of the average grain sizes in GNRs with different Pd loadings
9. Mobility calculation of GNRs

- Supplementary Figures S1-S13
- Supplementary references

Experimental section:

Materials

Palladium (II) acetate (99.98% trace metals basis), Poly(4-vinylphenol) (PVP, average M_w ~ 25,000), Tetrahydrofuran (anhydrous, >99.9%), Poly(methyl methacrylate) (PMMA, average M_w ~ 996,000), chlorobenzene (anhydrous, >99.9%), Myristyl Trimethyl Ammonium Bromide (MiTMAB) were purchased from Sigma-Aldrich and used as received.

Preparation of palladium-incorporated poly-4-vinyl phenol (Pd@PVP) solution

1.5 g PVP was dissolved in 5 ml THF. The mixture was stirred at room temperature for 3 hours for complete dissolution. Then, 4.5 – 45 mg/mL $Pd(OAc)_2$ and 0.05 g MiTMAB were added into the solution and stirred for another 10 min before electrospinning.

Electrospinning of (Pd@PVP) nanofibers

The aforementioned solution was loaded into a 3 ml syringe for electrospinning. The syringe was connected to a syringe pump (KDS200, KD Scientific Inc.), which maintained a steady flow rate of 0.2-1 ml/h during electrospinning. A high voltage (8 - 15 kV) was applied on the syringe needle and the collector substrate was grounded. The distance between the syringe tip and the collector was 10 - 15 cm. The random electrospun Pd@PVP nanofiber films were pulled out onto quartz or SiO_2/Si substrates under the electrostatic force. Figure S1 shows the SEM micrograph and its corresponding FFT pattern of the randomly distributed polymer nanofibers electrospun onto the wafer shown in Fig. 1c. The density of the Pd@PVP nanofibers is tuned by the electrospinning time.

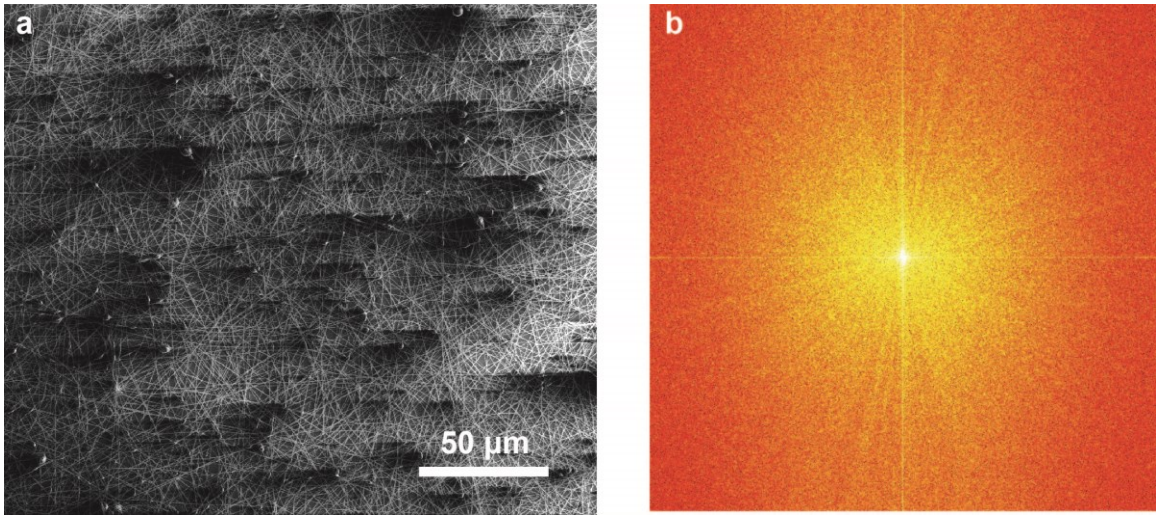

Figure S1. (a) SEM image of randomly distributed polymer nanofibers on the growth wafer as shown in Fig. 1c. (b) FFT pattern corresponding to (a).

CVD process

The electrospun nanofibers were then loaded into a low pressure CVD system. Prior to growth, the system was evacuated to a low pressure (~ 5 mTorr). Then, the temperature was slowly ramped up (~10 ˚C/min) to 1040 ˚C under the flow of 10 sccm H_2 (~ 80 mTorr). The temperature was maintained at 1040 ˚C for 30 min and 35 sccm CH_4 gas was introduced (~ 250 mTorr) as carbon source to grow GNRs. After the growth, the system was cooled down to room temperature under the flow of 10 sccm H_2 (~ 80 mTorr).

Morphology characterizations (scanning electron microscopy and atomic force microscopy)

To characterize the morphology of electrospun Pd@PVP nanofibers and post-CVD GNRs, we utilized both SEM and AFM. SEM was performed with an FEI Magellan 400 XHR scanning electron microscope operated at 5 kV, with a working distance of 4 mm. AFM was performed on a Digital Instruments Nanoscope in tapping mode. Tip-sample convolution is known to broaden the lateral features[1]. To correct for this broadening effect, we first used the same probe to image a carbon nanotube (CNT) sample (Fig. S2). We assumed that CNT is a cylindrical structure and the actual width is equal to the height. The measured width is broadened by the finite radii of the tip. The broadening can thus be calculated by $\Delta w = w - h$, where w and h are the measured width and height of the CNT respectively. For example, w and h measured from a CNT in Fig. S2 are 23.0 and

1.2 nm respectively and Δw is calculated to be 21.8 nm. This broadening can then be subtracted from the measured widths of the GNRs to estimate their actual widths.

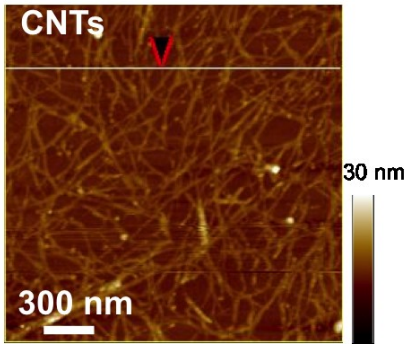

Figure S2. AFM images of CNTs for calibrating the tip broadening.

Structure and composition characterizations (Raman, TEM, XPS, EDS and EELS)

Raman characterization was carried out in a WiTec system with a laser of 532-nm wavelength, 4-mW power and ~700-nm spot size. The Raman intensity mapping was recorded in a 4 μm x 4 μm area with 30 scan lines in each direction. The integration time for each pixel is 0.2 s.

We utilized the aberration-corrected TEM to study the atomic structure of GNRs. To prepare the TEM sample, we first spin-coated PMMA solution (46 mg/ ml in cholorobenzene) onto the surface of as-grown GNRs on Si/SiO_2 substrates, and then used KOH solution (1 M in water) to release the PMMA/GNR stack from the substrate. Next, we scooped the suspended PMMA/GNRs film from the KOH solution and placed it onto a copper TEM grid with amorphous carbon coating. After drying in air for 30 min, PMMA was dissolved in acetone for 10 s and the GNRs were attached on top of the TEM grid. TEM imaging was performed at 80 kV using an FEI Titan system equipped with a spherical aberration (Cs) corrector in the image-forming (objective) lens. The images

were acquired using an Ultrascan 1,000 CCD camera. EELS (electron energy loss spectroscopy) and EDS (Energy Dispersive X-ray Spectroscopy) were recorded on a FEI Tecnai TEM with 200-kV acceleration voltage.

XPS was carried out with PHI 5000 Versaprobe equipped with monochromatic Al K source, pass energy of 1486.6 eV and a step size of 0.1 eV.

Electrical transport measurement

For resistivity measurement of GNRs, we first grew GNRs at low density on quartz substrates. An array of Ti/Pd electrodes (Fig. S3a) was then deposited on the post-growth substrate by photolithography, metallization and lift-off method. The device array was then examined under optical microscope and those devices with single GNRs crossing multiple ($\geq$ 4) electrodes (Fig. S3b) were chosen for electrical measurement. The four-probe resistances of individual GNRs were measured on a probe station using a semiconductor analyzer (Keithley 4200-SCS). We then measured the width, height and length of each ribbon and calculated the resistivity using the following formula:

$$\rho = R\,\frac{wd}{l}$$

where ρ is the resistivity in the unit of Ωm and w, d and l are the width, height and length of the measured ribbon respectively.

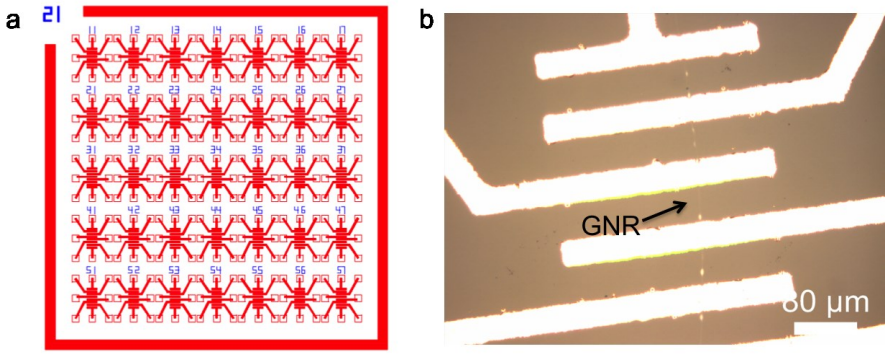

Figure S3. (a) Pattern of the photolithography mask for the electrode array for resistivity measurement. (b) Optical image of a single GNR crossing multiple electrodes.

To fabricate back-gated GNR-FETs, we first spin-coated a thin PMMA film as a carrier layer onto a Si substrate with 300-nm thermally-grown SiO_2 on top. PMMA film together with GNRs can be detached from the grown substrate by etching SiO_2 layer in hot KOH solution (1 mol/L) and transferred onto target substrate. E-beam lithography was used to pattern the source and drain electrodes. Then, we deposited Ti/Pd as electrode contacts. The Si back plane was used as the back gate. Electrical transport was recorded with the Keithley 4200-SCS semiconductor analyzer.

For low-temperature electrical measurements, the device chip was mounted on a ceramic chip carrier and the source and drain electrodes were wire-bonded to gold leads. The Si back plane was connected to a gold lead and grounded throughout the measurement. The chip carrier was then loaded into a Physical Property Measurement System (PPMS, Quantum Design) with a ^{4}He cryostat. The sample was first cooled down to 10 K then warmed up back to 300 K at rates of 5 K/min (< 140 K) and 10 K/min (> 140 K). The conductivity was measured at a constant current bias of 1 μA.

Other supporting information:

1. Optimization of the synthetic conditions for polymer-templated GNRs

The synthesis parameters are optimized to achieve long and narrow GNRs with uniform morphology and high crystallinity. To achieve this goal, we first studied the effect of the composition of the electrospinning solution. We found that lowering the concentration of PVP and addition of the MiTMAB surfactant favored the formation of polymer templates with small and uniform widths. The concentration of PVP and MiTMAB are fixed at 25 wt.% and 0.8% respectively for the results shown in the main text. The Pd^{2+} concentration was found to have a significant effect on the quality of the resultant GNRs, as discussed in the main text.

Next, we studied the effect of the CVD growth parameters. We observed that both the temperature ramping rate and the CH_4:H_2 ratio during CVD drastically affect the morphology of the GNRs. Slower ramping rate (12 ^oC/min) favors the formation of smooth and narrow GNRs, while faster ramping rate (33 ^oC/min) leads to thick ribbon structures with fibers protruding out of the surface (Fig. S4). We reason that during the temperature ramping stage, the PVP nanofibers undergo both vaporization and Pd-catalyzed graphitization. Both processes lead to the shrinkage of the width of the templates. A slower ramping rate thus leads to significantly smaller width of the resultant GNRs. Furthermore, slower ramping rate allows for sufficient time for the graphitization of the PVP template, and the graphitic domains formed during the ramping stage can serve as nucleation cites during the CVD stage (i.e. when CH_4 was fed into the growth system). On the other hand, with faster ramping there is insufficient time for the

graphitization of PVP, and during the CVD stage the CH_4 are more likely to react with the Pd nanoparticles to grow CNTs or carbon nanofibers following a vapor-liquid-solid (VLS) mechanism. This postulation is supported by the observation of bright particles at the end of the thin nanofibers in Fig. S4a.

We also found that higher CH_4:H_2 ratio during the growth favored the formation of smooth GNRs while higher H_2 concentration led to formation of pinholes on the surface of GNRs (Fig. S5). This can be attributed to the etching effect of H_2 on graphitic structures at high temperature[2].

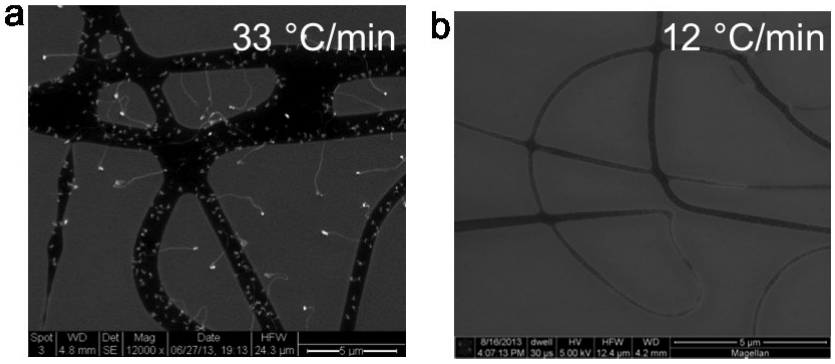

Figure S4. SEM images of GNRs from electrospun PVP at different CVD ramping speeds.

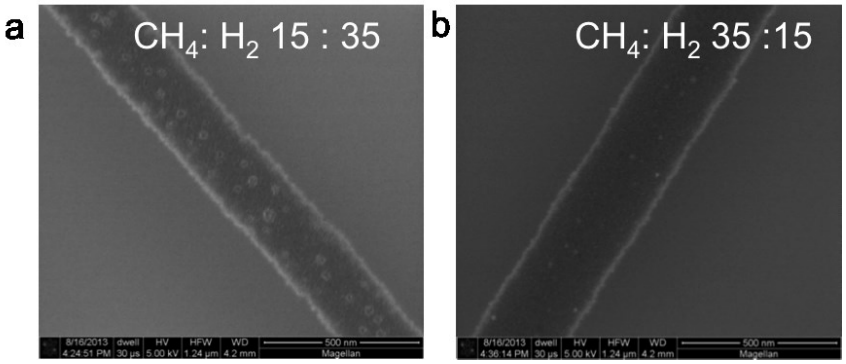

Figure S5. SEM images of GNRs from electrospun PVP at different gas ratios of methane and hydrogen during CVD growth.

2. CVD growth on Pd@PS nanofibers

To understand the role of Pd-phenol interaction, we performed CVD growth on Pd-incorporated polystyrene (Pd@PS) nanofibers under the same condition as the case in Pd@PVP. Importantly, no GNR was grown from the Pd@PS template. Instead, carbon nanofibers were formed with metal nanoparticles at the tips (Fig. S6). These carbon fibers were likely formed by a vapor-liquid-solid (VLS) process catalyzed by aggregated Pd nanoparticles. This result clearly shows that the Pd-phenol interaction is indeed crucial in stabilizing the Pd catalyst and enabling the GNR growth.

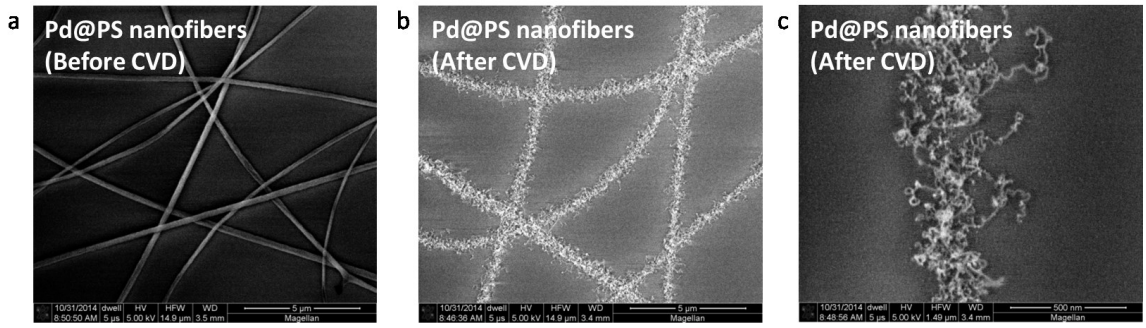

Figure S6. SEM images of Pd@PS nanofiber (a) and the CVD product (b, c).

3. The role of PVP

We performed the following experiments to address the role of the polymer.

1. Annealing of Pd@PVP nanofibers at the same temperature as CVD growth, but without CH4 supply. SEM images (Fig. S7a) reveals that ribbon-like structures were formed. However, we note that a large amount of fibers that root from the ribbon structures are also formed. These fibers all have nanoparticles at their tips, suggesting that they are formed by a vapor-liquid-solid (VLS) mechanism catalyzed by aggregated Pd nanoparticles. In fact, we have noticed in the CVD growth that a high CH_4:H_2 ratio needs to be used in order to prevent the formation

of such fibers. These observations indicate that, while CH_4 does not serve as the sole carbon source, it is critical for the formation of smooth GNRs.

2. Starting from plasma-treated Pd@PVP nanofibers. Fig. S7b and c show the SEM images of the plasma-treated nanofiber and the CVD product. Aggregated nanoparticles can be seen in the plasma-treated nanofibers. The CVD growth yield carbon fibers instead of GNRs, presumably following the VLS mechanism stated above. This result clearly indicates that the templating effect of the polymer nanofiber is crucial for the formation of GNRs.
3. Growth of GNR from poly(vinyl alcohol) template. Poly(vinyl alcohol) (PVA) contains no aromatic structures. We fabricated Pd-incorporated poly(vinyl alcohol) nanofibers (Pd@PVA) by electrospinning and performed CVD growth on them. The Pd concentration and CVD conditions are identical to those for Pd@PVP. We found that GNRs can indeed be synthesized (Fig. S7d); however, XPS analysis shows that the sp^2:sp^3 carbon ratio (~ 1:1) is much lower than GNRs synthesized from Pd@PVP templates (~ 3:1). Systematic investigation is underway to fully elucidate the role of the aromatic structures in the polymer template.

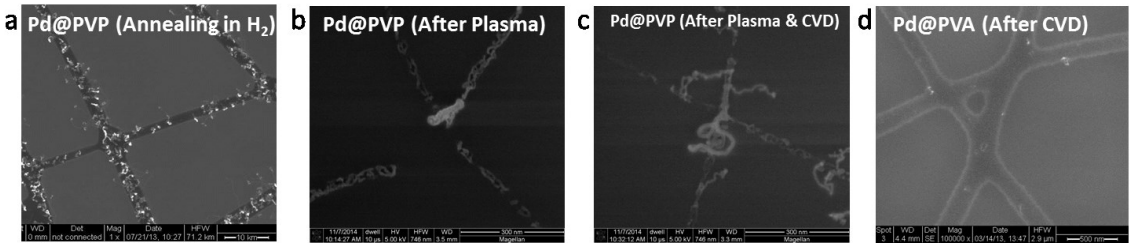

Figure S7. SEM images of Pd@PVP nanofibers annealed in H_2 (a), treated by O_2 plasma (b), and its CVD product (c). (d) SEM image of GNRs from Pd@PVA nanofibers.

4. Width comparison of electrospun polymer and GNRs at different concentrations of Pd catalysts

Figure S8 compared the widths of electrospun nanofibers and post-grown GNRs at different Pd^{2+} concentrations. With the catalysis of Pd, the resulted GNRs are narrower than the pre-CVD electrospun nanofibers. In contrast, without the catalysis of Pd, the polymer fibers melt into wider line structures and easily burnt away under high-energy electron beam during TEM imaging.

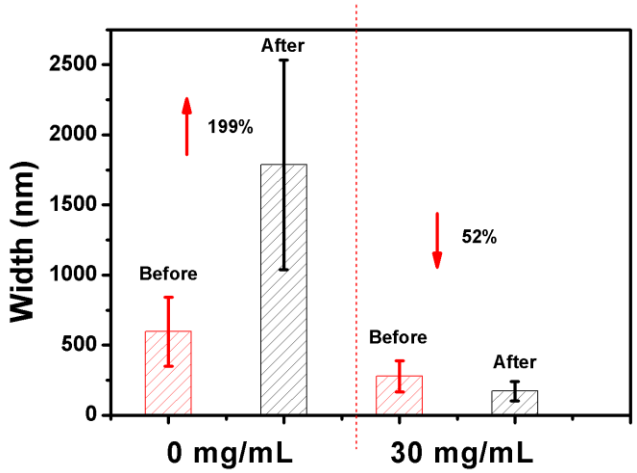

Figure S8. Width comparison of electrospun PVP and GNRs at different concentrations of $Pd(OAc)_2$. The widths are measured from SEM images and thus appear larger than those from AFM measurements. The changing trend is however unaffected.

5. Elemental analysis

EDS was used to analyze the elemental composition of Pd@PVP nanofibers electrospun on a silicon nitride membrane (Fig. S9).

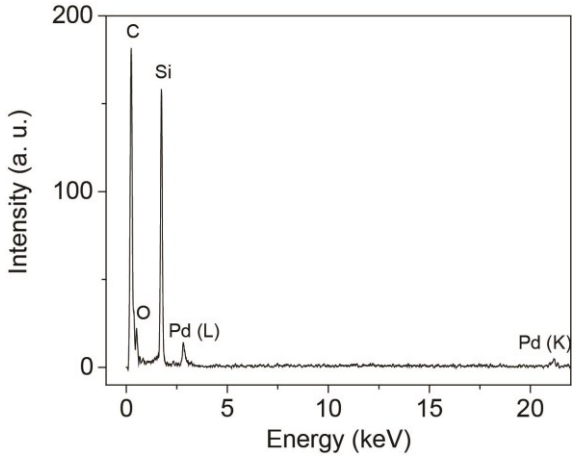

Figure S9. Representative EDS of Pd@PVP nanofibers showing the existence of C, O and Pd. The intensity of the spectrum is normalized to the Si peak.

We also used EELS to detect the presence of heteroatoms in GNRs grown on a silicon nitride membrane. The EELS result (Fig. S10) indicates that oxygen is indeed present in these GNRs. The oxygen atoms presumably originate from phenol group in the polymer template, the palladium acetate that was introduced as catalyst, or surface adsorption from air[3].

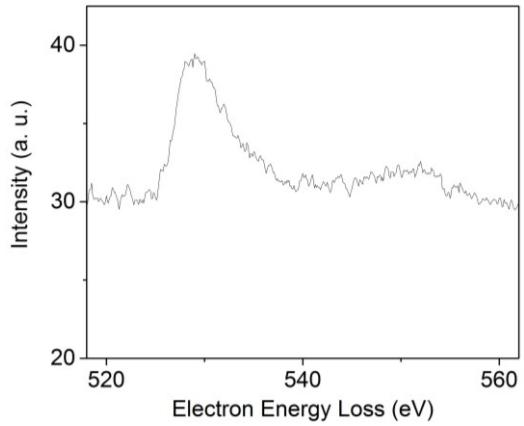

Figure S10. EELS of polymer-templated GNR showing the existence of oxygen.

6. Comparison of graphitization degree at different Pd^{2+} concentrations

XPS of the C1s core level is sensitive to the bonding configuration of the carbon atoms. We took C1s XPS spectra of GNRs on SiO_2/Si substrates with two different Pd^{2+}

concentrations in the electrospun solution (14 mg/mL and 20 mg/mL, Fig. S11). The baseline-subtracted XPS spectra can be fitted by two Voigt peaks centering at 284.2 (green lines) and 285 (blue lines) eV, which correspond to sp^2 and sp^3 carbon respectively[4]. The sp^2:sp^3 peak area ratio is 4.6 for the high-Pd-concentration sample and 2.9 for the low-Pd-concentration sample. The XPS data clearly shows the increased graphitization degree with higher Pd concentration, and further highlights the critical role of Pd catalysis.

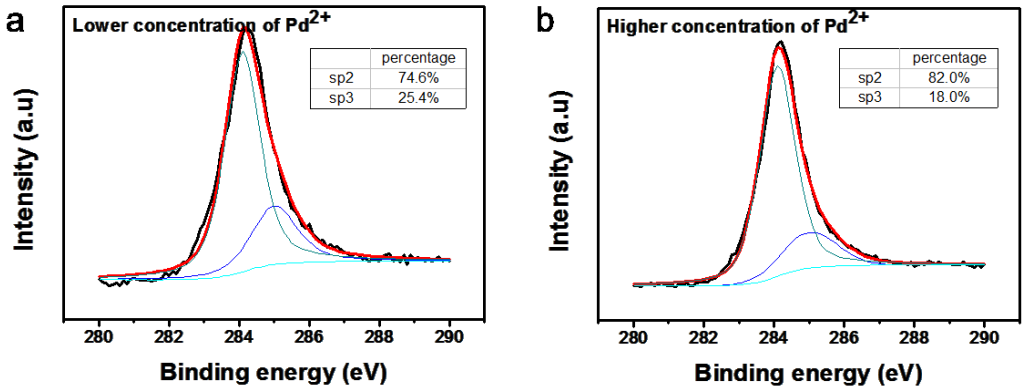

Figure S11. C1s XPS spectra of GNRs on SiO_2/Si substrates with two different Pd^{2+} concentrations of the electrospun solution (a: 14 mg/mL, b: 20 mg/mL). The black, red, green, blue and cyan curves correspond to the raw data, overall fit, sp^2 peak, sp^3 peak and baseline respectively. Fitting was performed with an XPS data analysis software (XPS Peak version 4.1).

7. Removal of Pd nanoparticles

We used aqua regia (HCl and HNO_3 in 3:1 volumetric ratio) at 50 ^oC for 30 s to etch Pd nanoparticles in GNRs. Energy-dispersive x-ray spectroscopy (EDS) result indeed shows

that the amount of Pd significantly decreases after etching (Fig. S12). We note that this etching process does not disrupt the 1D GNR structures.

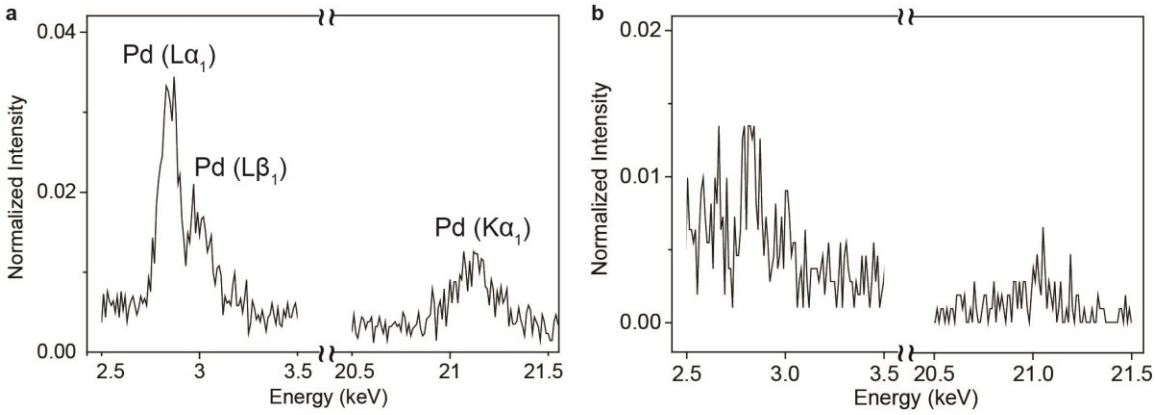

Figure S12. EDS of GNRs (a) as-grown and (b) after 30-s etching in aqua regia at 50 ^{o}C. The GNR sample is grown on a 15-nm silicon nitride membrane window. The peak intensities are normalized to that of silicon. The energy windows for the K- and L- lines of Pd are shown. Notably, the Pd peak intensities are substantially decreased and approaching sensitivity limit of the detector after the etching.

8. Analysis of the average grain sizes in GNRs with different Pd loadings

We use the Scherrer equation on the FFT patterns of representative TEM images to obtain the average domain sizes in the GNRs with different Pd loadings. We first took high-resolution TEM images on (1) GNRs without Pd, (2) GNRs with 9 mg/mL $Pd(OAc)_2$ loading, and (3) CVD graphene as a control (Fig. S13a, c and e). The FFT patterns of the TEM images (Fig. S13b, d and f) are integrated along the radial direction (Fig. S13g), and the full width at half maximum (FWHM) of the first peak (*100*) is used to calculate the average grain size by the Scherrer equation[5]:

$$D_{hkl} = 2\pi K/\Delta q_{hkl}$$

where D_{hkl} is the average grain size, K = 0.93 is the Scherrer constant, and Δq_{hkl} is the broadening (FWHM) of the scattering vector in reciprocal space. The FWHM of the (*100*) peak of the CVD graphene is taken as the instrumental broadening and subtracted from those of the GNR samples. Our calculation indicates the average graphitic grain size is 2.1 and 3.1 nm for GNRs without and with 9 mg/mL Pd loading respectively. The 50% increase of the domain size clearly reflects the critical role of Pd catalysis in the graphitization reaction, and is consistent with our conductivity measurement. It is worth noting that average grain size of the GNRs without Pd loading is likely overestimated by our method, since a large portion of these GNRs disintegrated immediately under electron beam and could not be imaged, suggesting even smaller or no graphitic domains in them.

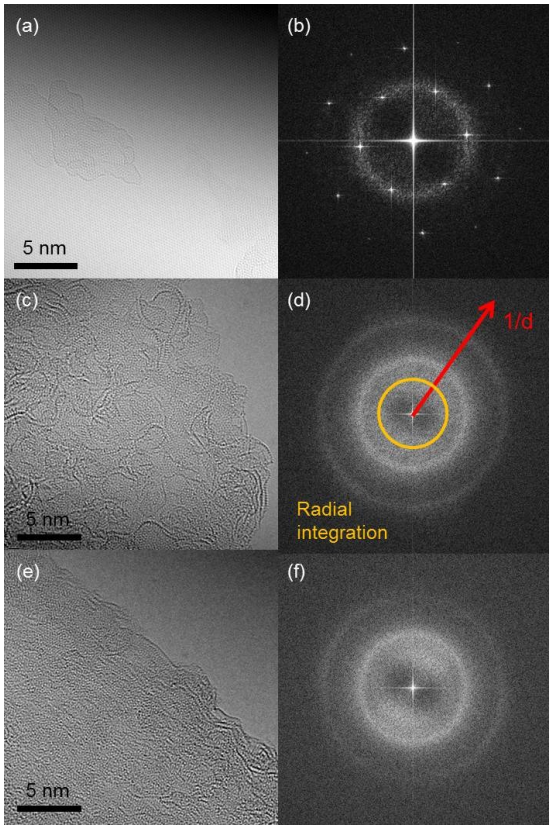

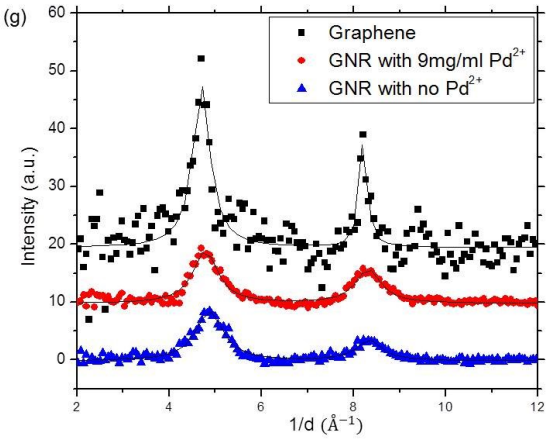

(h)

Sample	Peak width ($Å^{-1}$)	Grain size
Graphene	0.45	N/A
GNR with 9mg/ml Pd^{2+}	0.64	3.1 nm
GNR with no Pd^{2+}	0.72	2.1 nm

Figure S13. Analysis of graphitic domain sizes. (a, c, e) Atomic-resolution TEM images of CVD graphene grown on Cu foil (a), GNRs grown from electrospun Pd@PVP with Pd loading of 9 mg/mL (c) and without Pd (e). (b, d, f) FFT patterns corresponding to (a, c, e) respectively. (g) Intensity profile of the FFT patterns integrated along the radio direction. (h) Summary of (100) peak widths and grain sizes for CVD graphene, GNRs with and without Pd loading.

9. Mobility calculation of GNRs

The field-effect mobilities were derived from the linear regime of the I_{ds}-V_g curves, using the equation

$$\mu = \frac{L}{WCV_{ds}} g_m$$

where μ is the field-effect mobility, L and W are the channel length and width respectively, C is the gate capacitance and g_m is the transconductance. For the 54-nm-wide device, g_m was derived from linear fitting of the I_{ds}-V_g curve (Fig. 6b) in the range of -60 to 0 V. C was calculated using a planar capacitor model, assuming the dielectric constant and the thickness of the SiO_2 to be 3.9 and 300 nm respectively.

(1) Allen, M. J.; Hud, N. V.; Balooch, M.; Tench, R. J.; Siekhaus, W. J.; Balhorn, R., *Ultramicroscopy* **1992,** *42*, 1095-1100.
(2) Zhang, X.; Ning, J.; Li, X.; Wang, B.; Hao, L.; Liang, M.; Jin, M.; Zhi, L., *Nanoscale* **2013,** *5*, 8363-8366.
(3) Li, Z.; Wang, Y.; Kozbial, A.; Shenoy, G.; Zhou, F.; McGinley, R.; Ireland, P.; Morganstein, B.; Kunkel, A.; Surwade, S. P.; Li, L.; Liu, H., *Nat. Mater. 12*, 925-931.
(4) Sokolov, A. N.; Yap, F. L.; Liu, N.; Kim, K.; Ci, L.; Johnson, O. B.; Wang, H.; Vosgueritchian, M.; Koh, A. L.; Chen, J., *Nat. Commun.* **2013,** *4*. Article Number: 2402.
(5) Smilgies, D.-M., *J. Appl. Crystallogr.* **2009,** *42*, 1030-1034.